

D. Flynn · Nirmal Singh Sudan · A. Toon  
M. P. Y. Desmulliez

## Fabrication process of a micro-inductor utilising a magnetic thin film core

Received: 1 August 2005 / Accepted: 28 October 2005 / Published online: 11 April 2006  
© Springer-Verlag 2006

**Abstract** Thin film magnetic alloys incorporated into microscale magnetic components are investigated as a potential solution to the increased power density required in power supplies of fast switching frequencies. The performances of direct current and Pulse Reverse (PR) electrodeposited permalloy and Vitrovac 6025 are assessed through their inclusion within a solenoid microinductor. A design of experiment (DOE) determined the optimum waveform for (PR) deposition within a sulphate electrolyte. The effects of air-gaps on core performance are also investigated. The fabricated inductors have an inductance ranging from 0.12 to 118  $\mu\text{H}$ .

### 1 Introduction

Magnetic components continue to be an essential element in power conversion and management circuits. Improving their performance in order to meet the market is only possible by addressing every aspect of the device from winding configuration, material development for improved magnetic core performance and fabrication process for reduced size and packaging.

The need for faster switching, reduced losses and smaller components have driven switching frequencies into the range of 0.5–10 MHz (van Wyk and Lee 1999; Huljak et al. 2000; International technology roadmap for semiconductors 2001; Lotfi and Wilkowski 2001).

The limitation in going to higher switching frequencies lies in the loss of current magnetic components with frequency. Ferrites appeared to have reached their limits in terms of higher frequency operation at reasonable loss levels. With increasing frequency, the magnetic component becomes smaller, ac resistance losses increase and current handling capability is becoming more stringent. Hence, typical ferrite cores, whose useable flux density falls drastically at these higher frequencies, have to be replaced and a method of producing small windings developed. New core materials must have high resistivity, and high saturation flux, permeability of 100–3,000, low coercivity and be suitable for thin film deposition.

As power consumption goes up and device size comes down, engineers are looking at new ways to design power supplies. Battery power life can be a deciding factor in a consumer's choice of portable device, while it can also determine the extent of functionality of the device itself. So, clearly power supplies and semiconductors need to be small and efficient.

In this work, a solenoid microinductor is fabricated by the UV LIGA process. In order to assess the suitability of Vitrovac 6025 and Permalloy as magnetic materials, samples of both materials have been assembled within a microinductor and tested over a frequency range of 1 kHz to 13 MHz. Results indicate the major loss mechanisms that need to be minimized at high frequency for magnetic components, and the desirable properties of an optimal thin film core.

### 2 Inductor design

The fabricated structure is displayed in Fig. 1. The solenoid structure was chosen because: the fabrication process permitted the comparison of various core materials within the same component, magnetically efficient, biasing the magnetic core to create magnetically anisotropic films is straightforward, most of the fields produced by the solenoid are in the plane of the core, and eddy currents can be controlled by varying

D. Flynn (✉) · N. S. Sudan · M. P. Y. Desmulliez  
MISEC, School of Engineering & Physical Sciences,  
Heriot Watt University, Edinburgh EH14 4AS, UK  
E-mail: df2@hw.ac.uk  
Tel.: +44-131-4513774  
Fax: +44-131-4514155

A. Toon  
Raytheon Systems Limited, Queensway Industrial Estate,  
Glenrothes, Fife KY7 5PY, UK

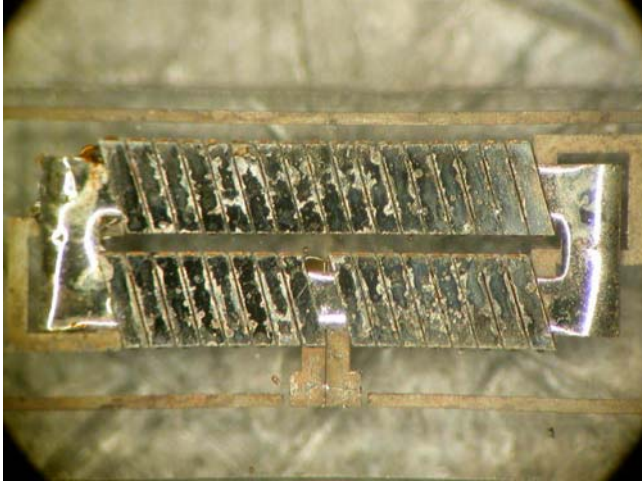


**Fig. 1** Fabricated micro-inductor of size 2 mm×5 mm×250 μm ( $W \times L \times T$ ). The nickel windings are clearly visible diagonally. The Ni(80)Fe(20) core of O-shape is assembled between the windings by flip-chip bonding

the thickness of the core. The disadvantage of this structure includes a possible large distributed capacitance in the structure due to the number of windings. The relatively complex structure with multiple contacts could lead to increased resistance which would reduce the quality factor (Q).

The circuit equivalent of the inductor is a series resistance  $R_T$  and inductance  $L_T$  both in parallel with a capacitance  $C$ . The first two parameters take into account the skin and proximity effects in the windings and eddy currents within the magnetic core. The parallel capacitance models the parasitic capacitance that emanates between turns, turns to insulation layer, and turns to core.

The series inductance consists of the main inductance,  $L$ , and the leakage inductance of the windings. The latter can usually be neglected (Kazimierczuk et al. 1999). The expressions of the inductance  $L$  and the reluctance  $R$  of the inductor of Fig. 1 are:

$$L = \frac{(\mu_0 \mu_r A_c N^2)}{l_c} = \frac{N^2}{R} \quad (1)$$

$$R = \frac{l_c}{\mu_0 \mu_r A_c} \quad (2)$$

where  $A_c$  is the cross-sectional area of the magnetic core,  $l_c$  is the length of the closed magnetic path,  $N$  is the number of coil turns,  $\mu_0$  and  $\mu_r$  are the permeability of free space and the relative permeability of the magnetic core, respectively. To avoid magnetically saturating the device, the maximum current that can be applied,  $I_{sat}$ , is:

$$I_{sat} = \frac{B_{sat} R A_c}{N} \quad (3)$$

$B_{sat}$  is the flux density at which the magnetic core saturates. An air-gap has been patterned into the two magnetic samples. This increases the reluctance of the

magnetic path, reduces the inductance but increases the saturation current through the effective permeability,  $\mu_e$ , of the device with an air-gap core:

$$\mu_e = \mu_0 \mu_r \frac{l_c}{l_c + \mu_r l_a} \quad (4)$$

with  $l_a$  being the length of the air-gap. With the value of saturation current known, and for a fixed value of the current density (10 A/mm<sup>2</sup> typically for PCB), the winding area can be determined to handle the saturation current.

In order to minimize eddy current losses in the core and windings at high frequency, the skin depth,  $d$ , has to be known. Thicknesses that are greater than skin depth at the frequency of operation will create greater losses. The equation for skin depth is:

$$d = \sqrt{\frac{1}{\mu_0 \mu_r f \pi \sigma}} \quad (5)$$

where  $f$  is the operating frequency and  $\sigma$  is the conductivity of the material. The increase in AC resistance,  $R_{ac}$ , within the windings can be determined by:

$$\frac{R_{ac}}{R_{dc}} = 1 + \frac{\psi}{3} \Delta^4$$

$$\Psi = \frac{5p^2 - 1}{15} \quad (6)$$

$$R_{dc} = \rho \frac{l}{A_w}$$

where  $p$  is the number of winding layers, and  $\Delta$  is the ratio of winding thickness to skin depth (Hurley et al. 2000),  $A_w$  is the area of the winding and  $\rho$  is the resistivity of the winding material. Eddy currents within the core increase the series resistance according to the relation (Grandi et al. 2004; Kazimierczuk et al. 1999):

$$R_c = \omega L \left( \frac{d_c}{t} \right) \times \left( \frac{\sinh(t/d_c) - \sin(t/d_c)}{\cosh(t/d_c) + \cos(t/d_c)} \right) \quad (7)$$

with  $\omega$  the radian frequency of operation,  $d_c$  the core skin depth at that frequency, and  $t$  the thickness of the core layer.

### 3 Fabrication of thin film core

Core samples were fabricated on separate wafers to permit electrical and magnetic characterization prior to inclusion within the component. The Ni(80)Fe(20) samples were fabricated by DC and PR electrodeposition. The composition of the electrolyte for both waveforms is given in Table 1. The anode is Nickel and the only variable during the DC deposition was current density. The Vitrovac 6025 foil was patterned with AZ 9260 and wet etched to the desired dimensions. The etchant consists of HNO<sub>3</sub>:HCl:H<sub>2</sub>O, 2:1:3.

**Table 1** Composition of NiFe plating solution

Component	Concentration
NiSO <sub>4</sub>	0.7 (mol/l)
FeSO <sub>4</sub>	0.03 (mol/l)
NiCl <sub>2</sub>	0.02 (mol/l)
Boric acid	0.4 (mol/l)
Saccharin	0.016 (mol/l)
pH	2.5–3.0
Temperature	25–30 (°C)

The PR waveforms were developed from a design of experiment (DOE) based on five parameters, Fig. 2: (a) cathodic current density, (b) cathodic pulse time, (c) anodic current density, (d) anodic pulse time and (e) off-time. Limitations in frequency, current density and anodic to cathodic ratio provide a maximum and a minimum value for each parameter. The full factorial analysis produces 32 potential waveforms of which 25 were valid. A 10 µm deposit was produced by each waveform. The definition of each waveform parameter is as follows:

$$\text{Frequency } F = \frac{1}{\lambda} \text{ (Hz)} \quad (8)$$

where,  $\lambda = b + d + e$ ,

$$\text{Average current density } I = \frac{(x + y)}{\lambda} \quad (9)$$

where,  $x = a*b$  and  $y = c*d$ ,

$$\text{Current ratio, } R = \frac{c}{a} \quad (10)$$

$$\text{Off-time } t_{\text{off}} = e \quad (11)$$

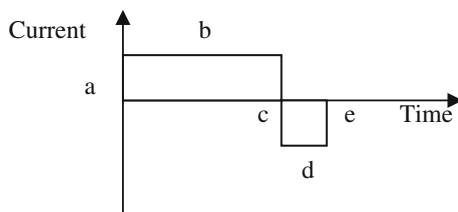
$$\text{Positive duty cycle } \partial^+ = \frac{b}{\lambda} \times 100\% \quad (12)$$

$$\text{Negative duty cycle } \partial^- = \frac{d}{\lambda} \times 100\% \quad (13)$$

On duty cycle

$$\partial^{\text{on}} = \frac{(b + d)}{\lambda} \times 100\% = \partial^+ + \partial^- \quad (14)$$

The background conditions kept constant are: concentration of metal salts, conductive salts and buffering agents, bath temperature, agitation rate, solution pH, plating cell geometry, composition and condition of anodes, anode/cathode surface area ratio, and nature and condition of substrate (seed layer).

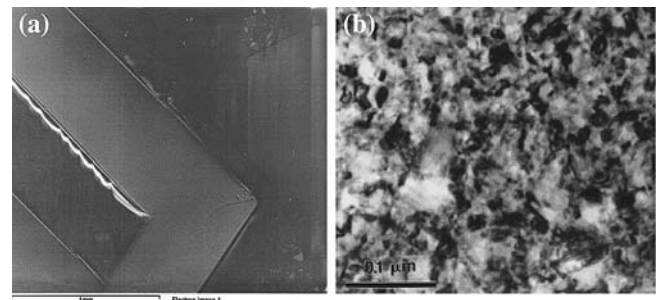
**Fig. 2** Pulse reversal (PR) waveform

The NiFe composition is determined with energy dispersive X-ray analysis (EDX)-scanning electron microscope (SEM). SEM and transverse electron microscope (TEM) images analyze the surface of the deposit. Deposition rate is recorded with white light interferometer. XRD data displays the crystal structure of the film. Atomic force microscope (AFM) data records surface roughness and grain size. Resistivity is measured with a 4-point probe and the magnetic properties are obtained with a vibrating sample magnetometer (VSM).

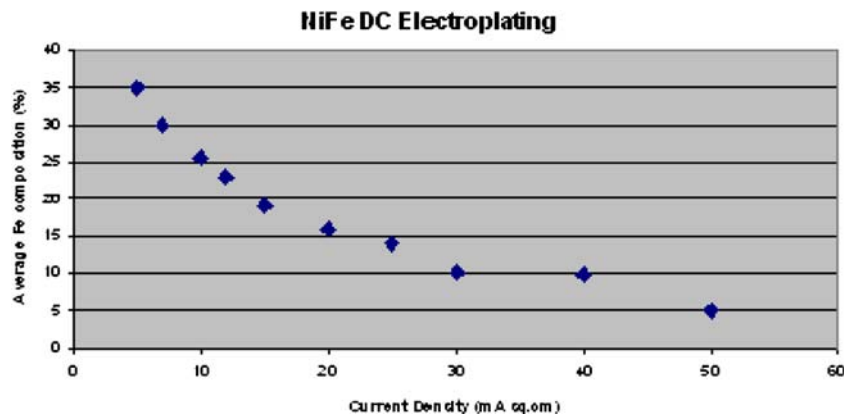
### 3.1 Experimental results and analysis of nickel: iron

Scanning electron microscope (SEM) images of the DC and PR Ni(80)Fe(20) deposit show them to have smooth morphology and to be defect free. An example of the PR permalloy is displayed in Fig. 3a. However, the TEM image of the PR sample, Fig. 3b, shows the detailed structure in the film. The film consists of NiFe nanocrystallinities with diameters ranging from 10 to 50 nm.

Variation of current density with the DC waveform resulted in anomalous co-deposition, as recorded with EDX-SEM, Fig. 4. This term, introduced by Brenner (Activities of the PFM on permalloy thin films deposition and magnetic devices 2000; Matlosz 1993; Sasaki and Talbot 1995), describes the preferential deposition of the less noble metal, Fe, to the more noble metal, Ni. The Fe content for the DC deposition reached a maximum then decreased with increasing average current density. This type of behavior is characteristic of systems which exhibit anomalous co-deposition. Dahms and Croll surmised that iron hydroxides, which form as a result of the rise in pH at the cathode during co-deposition of hydrogen, inhibit nickel deposition resulting in anomalous co-deposition (Brunet et al. 2001). In view of this a small sample of the electrolyte was withdrawn with a syringe in order to measure the pH. The pH increased from 2.5 in the bulk of the solution to 6 near the cathode. The accuracy of the actual value is questionable since

**Fig. 3** a Scanning electron microscope (SEM) image of Ni(80)Fe(20) sample. b Transverse electron microscope (TEM) image of the same sample

**Fig. 4** Anomalous co-deposition effect of DC electroplated NiFe



disturbing the electrolyte will affect the build-up of species at the cathode.

As shown in Fig. 4 a current density of approximately 15 mA/cm<sup>2</sup> achieves the 80:20 compositions for the DC waveform.

The DC deposits exhibit current crowding, Fig. 5, indicated by the upward slope in the corner of the deposit. PR plating preferentially removes deposit from areas of over-plating reducing the effect of current crowding (see Fig. 6).

The effect of varying PR waveforms on the structure of the NiFe deposit was observed in terms of pitting, plating efficiency, composition, resistivity, hysteresis and grain size. Pitting within the core can result in unpredictable inductance and losses due to variations in flux density. The effect of cathodic pulse density on pitting has been recorded in Fig. 7. Figure 7 displays that a zero pit count is possible in the dark blue region denoted by the corresponding values of *a* in amperes and *b* in milliseconds.

A contour plot is shown in Fig. 8 displaying the relation between average current  $I_{avg}$ , the average pit count and wavelength.

Figure 8 indicates that as the average current density increases in the 0.25–0.37 A/cm<sup>2</sup> range the wavelength

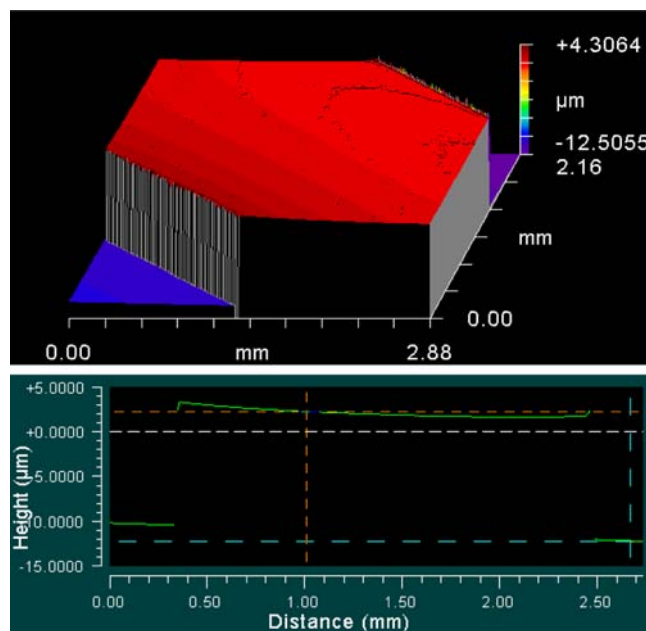


**Fig. 6** Fe 15% PR deposit with improved surface uniformity

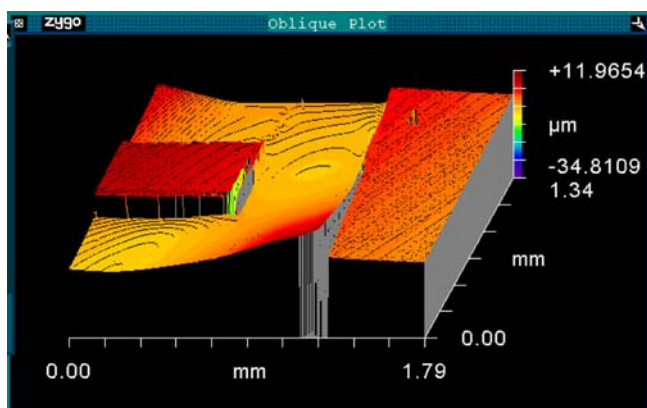


**Fig. 5** Fe 15% DC deposit exhibiting the effects of current crowding

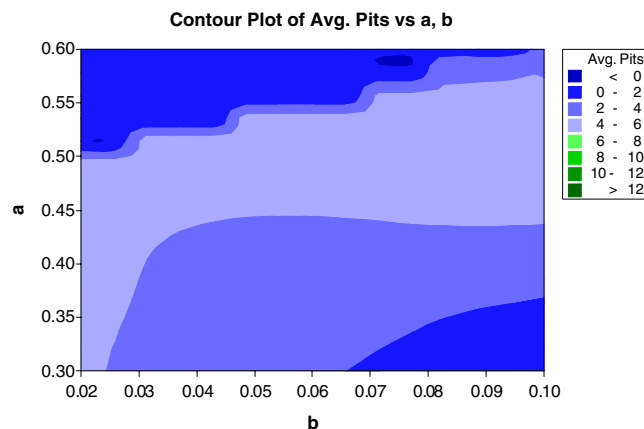


**Fig. 7** Average pit count versus pulse duration and pulse density



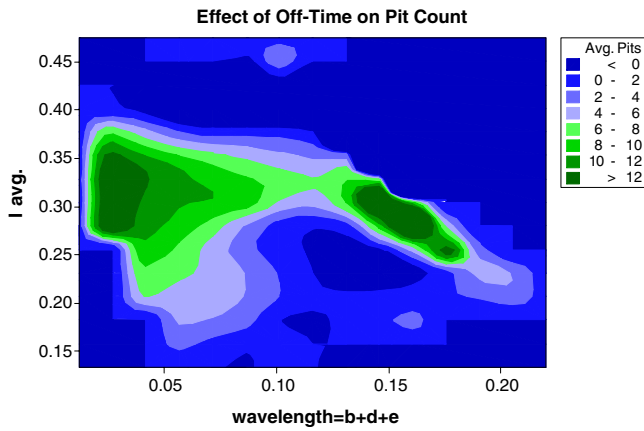


Fig. 8 The effect of off-time on pit count

must also increase to reduce the number of pits. It is surmised that the off-time allows the mass transfer to replenish the ions at the cathode surface. Therefore to reduce off-time promotes the evolution of hydrogen.

Anodic pulse density, Fig. 9, also plays an important role in pitting. If the Anodic pulse is greater than a tolerable level it results in pitting. In some cases when the anodic pulse was too great Ni was removed from the Ti/Ni seed layer.

From the contour plot, Fig. 9, it can be clearly seen from the blue areas that the least amount of pits occurs in the region of the anodic pulse duration being less than 10 ms. It is evident from first principles that the cathodic pulse density must be greater than the anodic in order to form a deposit. Figure 10 also demonstrates that the lowest pit count is obtained if the value of  $x$ , cathodic current density, lies between 0.04 and 0.06 and  $y$ , anodic current density, lies between 0.005 and 0.010. Any increase in the value of  $y$  above 0.010, results in increased average pit count.

With an increase in current density it is anticipated that there would be a reduction in grain size. However this is not always the case. Figure 11 highlights that as

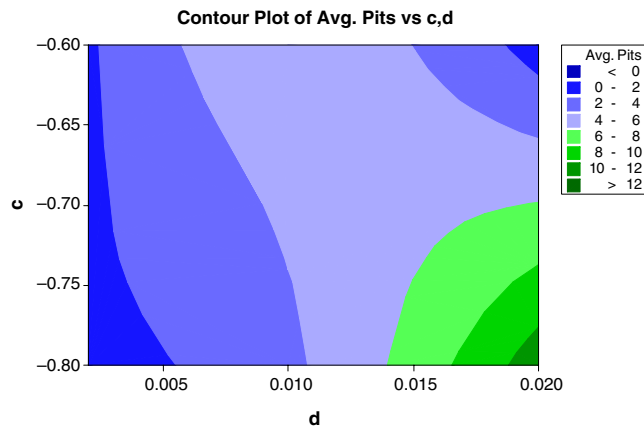


Fig. 9 A contour plot of the average number of pits per sample against the anodic pulse amplitude ( $c$ ) and the anodic pulse duration ( $d$ )

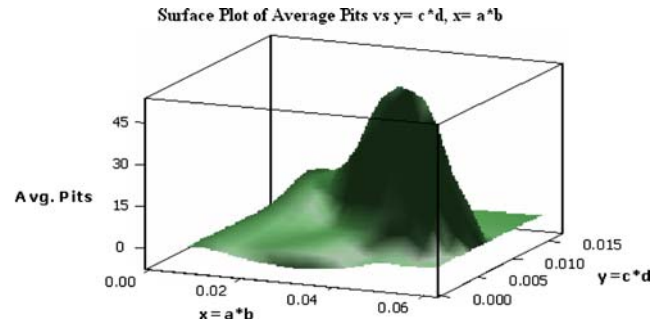


Fig. 10 Surface plot of average pits versus  $x$  and  $y$

the current density increases with some waveforms the roughness increases. This could be the result of an increase in grain size.

Atomic force microscope (AFM) scans of deposits allowed measurement of grain sizes, Fig. 12. A waveform that produced a permalloy composition with good deposit quality is analyzed below. The current density of  $0.2 \text{ A/cm}^2$  produced a grain size of 10.797 nm. The DC permalloy sample fabricated at  $15 \text{ mA/cm}^2$  consisted of an average grain size of 136 nm. Also the grain size is consistent throughout the PR films thickness unlike the

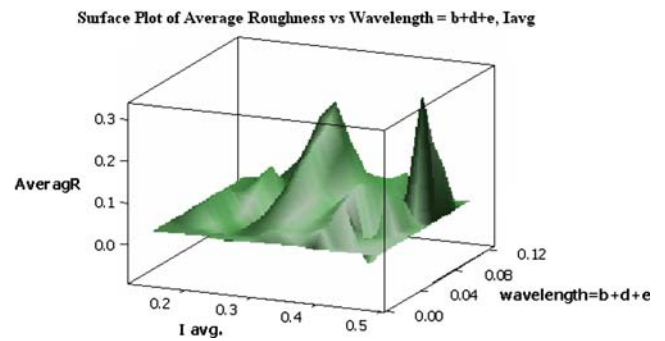


Fig. 11 Average roughness versus wavelength and current density

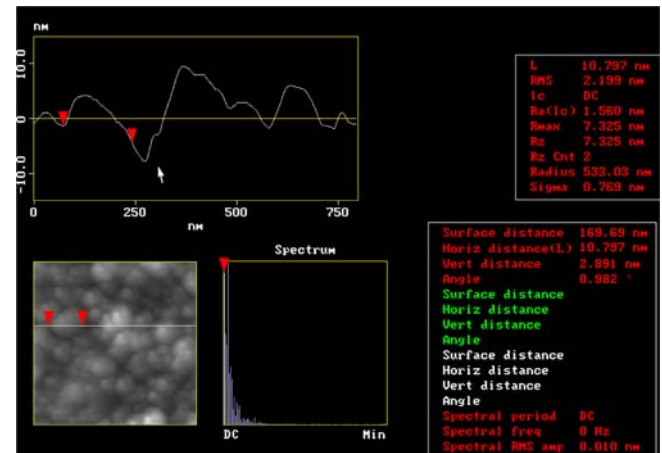


Fig. 12 Atomic force microscope (AFM) data of Ni(80)Fe(20) sample

DC plating that exhibits coursing with increased film thickness.

From Fig. 13 it is seen that the iron content increases in the sample when  $y$  is between 0.005 and 0.010 and when  $x$  is between 10 and 20. Therefore to attain permalloy a high cathodic to anodic pulse density ratio is required. A waveform of  $a=0.4$  mA,  $b=100$  ms,  $c=-0.6$  mA,  $d=10$  mS and  $e=10$  mS resulted in Ni(80)Fe(20). The maximum iron content is a lot lower than DC at a far greater maximum current density.

Theoretically there is a linear relationship between the charge applied and thickness of the deposited film described by

$$Q = tADn \frac{F}{M} \quad (8)$$

Taking the plating area  $A$  in square centimeters, permalloy density  $D=8.60$  g/cm<sup>3</sup>, electrons involved in the reaction  $n=2$ , Faraday constant  $F=96,500$  C/mol, and the molecular weight of Ni(80)Fe(20)  $M=58.1$ , the charge  $Q$  necessary to produce a film of thickness  $t$  can be calculated. Comparing the theoretical deposit thickness to the actual deposit thickness the efficiency can be determined. In this study the efficiency of the DC waveform was 84–86%. The PR waveform varied from 75 to 90%. The inefficiency is attributed to the co-evolution of hydrogen and possibly the reduction of oxygen in solution during the electrodeposition process.

XRD analysis, Figure 14, of DC and PR samples confirms that the crystal structures are face centre cubic (FCC). Nickel and iron are 100% soluble and are expected to have FCC structure in the composition range investigated.

XRD analysis also provides information on the lattice strain and lattice parameter. Figure 15 presents the variation in lattice strain as a function of the iron content of the deposits. The lattice strain increased with the iron content of the deposits.

There may be a correlation between the reduction in grain size and the increase in the internal stresses. However the variation in grain size was a matter of a few percent in some cases. Surface diffusion plays an important role on the development of defects in elec-

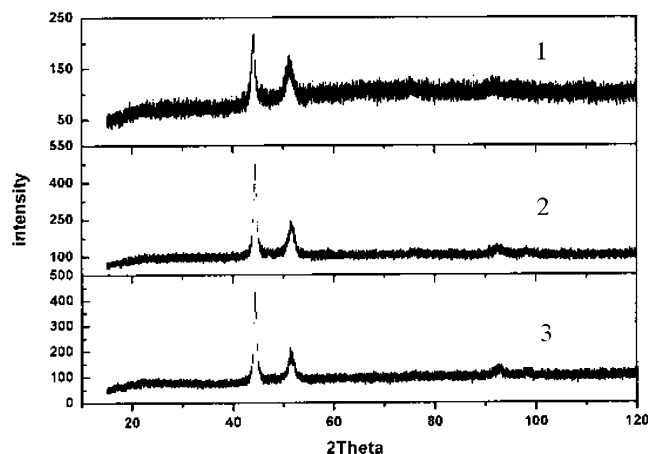


Fig. 14 XRD spectrum of Ni:Fe samples with varying composition (1) 75.34:24.65 (2) 76.27:23.73 (3) 83.31:16.69

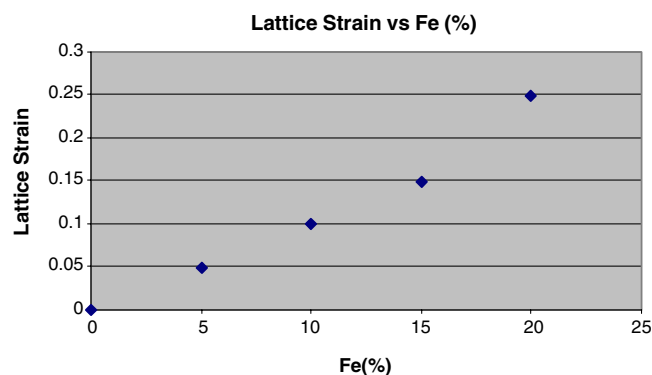


Fig. 15 Iron concentration versus  $x$  and  $y$

trodeposits. Should the iron concentration of the bath deplete to the point where it effects the surface diffusion; a more defective structure with higher internal stresses is expected to develop.

Figure 16 displays the variation of lattice parameter with iron content. The increase in the lattice parameter with increase in iron is similar to the behavior observed in conventional well annealed and electrodeposited FCC Ni-Fe alloys.

It has been suggested that the level of the internal stresses in NiFe electrodeposits is due to the lattice mismatch between the deposit and the substrate. However the copper substrate has a larger lattice parameter,  $Cu=3.6150$ , than the permalloy. Increasing the iron content increases the lattice parameter of the NiFe nearer to that of Cu, so in fact should reduced the internal stress. However, opposite to this the stress actually increases.

#### 4 Fabrication of the microinductor

The solenoid structure of this component involves the assembly of three separate wafers. The fabrication of upper and lower winding layers, with the third wafer

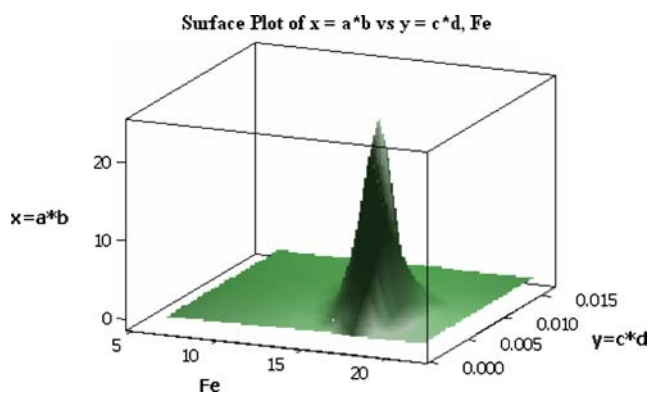


Fig. 13 Iron concentration versus  $x$  and  $y$

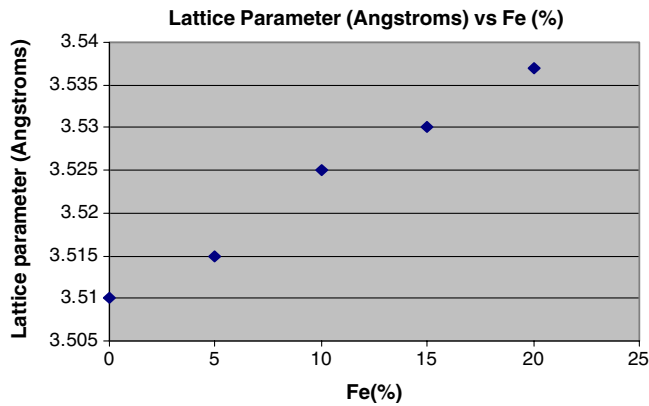


Fig. 16 Iron concentration versus  $x$  and  $y$

contains the core of the component. A summarized fabrication process is given below:

- Step 1 A 3-in. glass wafer is immersed in deionized water and cleaned for 3 h within an ultrasonic bath.
- Step 2 A titanium adhesion layer, 100–200 nm thick, is deposited within an electron beam evaporator. A uniform electroplate across the surface of the wafer requires the reduction in the resistivity of the seed layer. Hence, a 100–200 nm thick layer of a more conductive metal such as Ni or Cu is deposited.
- Step 3 A positive photoresist AZ 9260 is deposited to obtain the required conductor and core thickness.
- Step 4 AZ 9260 patterned with UV light using an acetate mask in a contact exposure mode.
- Step 5 The upper and lower winding layers are DC electroplated with either Cu or Ni.
- Step 6 AZ is re-deposited and patterned, and gold bumps are electroplated. The seed layer is etched and AZ insulation is deposited and patterned, Fig. 17 displays the 3D plot and component image.
- Step 7 Magnetic core is electroplated and etched free. The upper and lower windings are diced.
- Step 8 The core is placed on the lower windings and the upper layer is flipped chip bonded, as shown in Fig. 18.
- Step 9 Ti etchant is used to release the glass substrate off the upper layer by etching the remainder of the upper seed layer, Fig. 19. The final component with 90  $\mu\text{m}$  thick windings has dimensions 5 mm  $\times$  2 mm  $\times$  0.25 mm.

## 5 Electrical and magnetic characterisation of the thin film core

The permalloy core has been released from the wafer and magnetically characterized within a vibrating sample

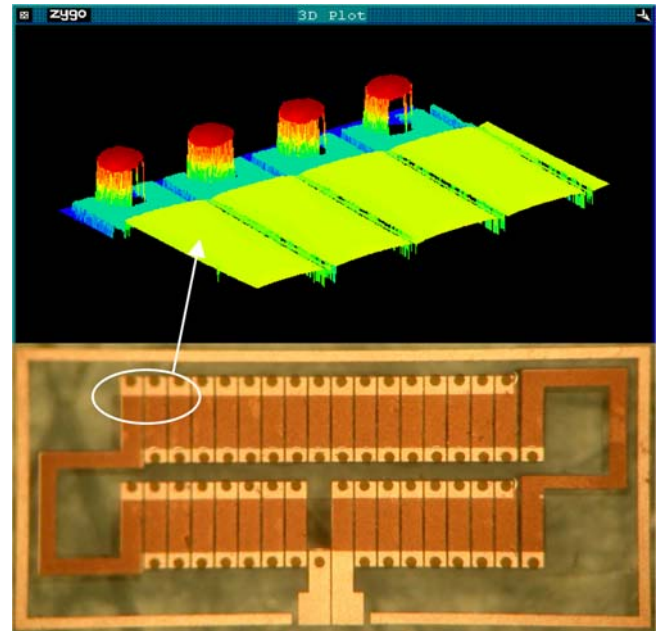


Fig. 17 Microinductor prior to core inclusion and flip chip bonding

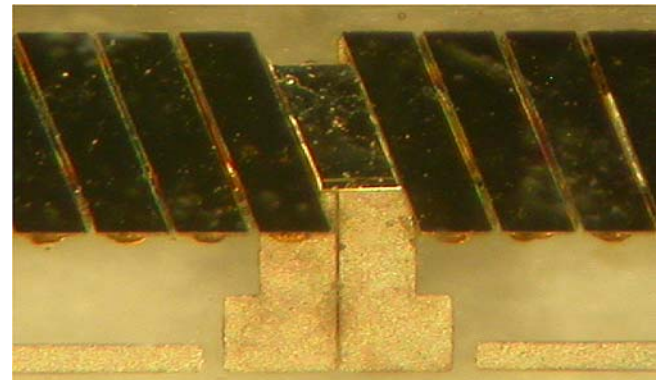


Fig. 18 Component after flip chip bonding. The view is through the upper glass substrate displaying the dark Ti seed layer

magnetometer (VSM), as shown in Fig. 20. The hysteresis curve provides the main data points that determine the film performance, i.e. the saturation flux density  $B_{\text{sat}}$ , maximum applied field  $H_{\text{sat}}$ , coercivity  $H_{\text{c}}$ , remance  $B_{\text{r}}$  and the permeability  $\mu$ . The resistivity of the film is obtained with a four-point probe. Manufacturer data provided all the necessary information for the Vitrovac sample (V6). The parameters utilized in the theoretical calculations are contained in Table 2.

The reduction in coercivity and increase in resistivity of the PR deposit is attributed to the reduced grain size. The reduced grain size leads to an increase in grain boundaries increasing the resistivity. As the average grain size approaches that of critical magnetic length scales (such as the domain wall thickness or the ferromagnetic exchange length) found in conventional



**Fig. 19** Glass substrate removed from the upper layer, some residual Ti has remained on the winding

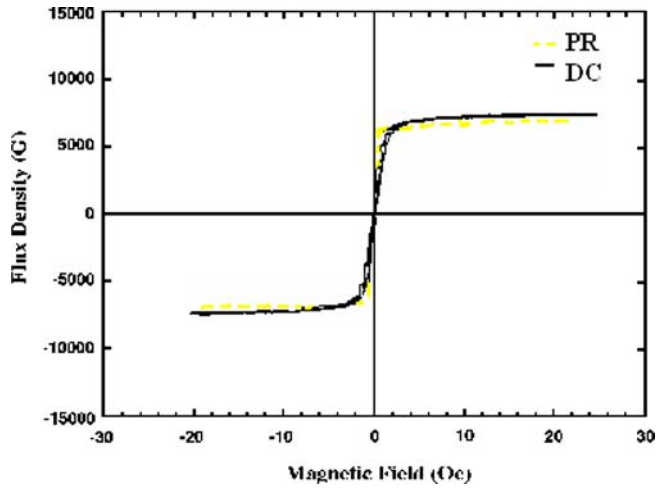
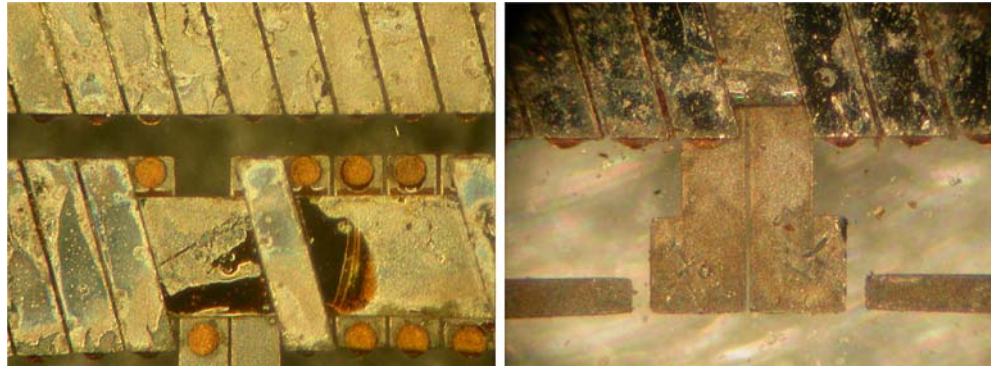


**Fig. 20** Hysteresis curve of permalloy

**Table 2** Ni(80)Fe(20)DC, Ni(80)Fe(20)PR and Vitrovac 6025 properties

Property	NiFe	PR-NiFe	6025 V
Resistivity ( $\rho$ in $\mu\Omega$ cm)	20	46	135
$B_{sat}$ (T)	0.85	0.79	0.55
Relative permeability ( $\mu_r$ )	$\approx 2,000$	$\approx 3,130$	$\approx 90,000$ – $100,000$
Core thickness ( $\mu\text{m}$ )	20, 10	10	20
Gap length ( $\mu\text{m}$ )	50	*	50
Width of core ( $\mu\text{m}$ )	500	500	500
Number of turns	33	33	33

materials, considerable changes in the magnetic behavior can occur. When the grain size is reduced to the extent of the domain wall thickness, the coercivity is found to dramatically decrease (Herzer et al. 1990).

## 6 Preliminary testing of the microinductor

A critical point in the performance of an inductor is the measurement of the inductance value as a function of frequency and the additional core losses. A Hewlett Packard 4192A LF impedance analyzer was used to record the inductance, resistance, Q-factor, impedance and

phase over a frequency range of 1–13 MHz. Seven components were fabricated with inductance values at 1 kHz of 118  $\mu\text{H}$  (V6), 0.27  $\mu\text{H}$  (V6 air gap), 2.48  $\mu\text{H}$  (NiFe-20  $\mu\text{m}$ ), 0.24  $\mu\text{H}$  (NiFe-20  $\mu\text{m}$ -air gap), 1.24  $\mu\text{H}$  (NiFe-10  $\mu\text{m}$ ), 0.12  $\mu\text{H}$  (NiFe-10  $\mu\text{m}$ -air gap) and 1.94  $\mu\text{H}$  (NiFe-10  $\mu\text{m}$ , PR).

The resistance values shown in Fig. 21 are for an air-core component. The thicker windings have a lower resistance  $R_{dc}$  at low frequency. However, when the operating frequency increases the skin effect results in a greater resultant resistance. The theoretical  $R_{dc}$  collates to the experimental value therefore the flip chip bonding method has removed the problem of increase resistance caused by vias.

The increase in resistance due to eddy currents is displayed in Fig. 22 for permalloys with different air gaps and Vitrovac. Thinner laminations control the onset of eddy currents and, as a consequence, present a smaller resistance for a given frequency. The introduction of the air gap interrupts the flow of eddy currents and therefore reduces the resistance. Although Vitrovac has a resistivity six times greater than permalloy, the extremely high permeability of the film makes it highly susceptible to eddy currents. The increase in resistance due to eddy currents is displayed in Fig. 22b. The PR deposit performance is degraded in the same manner with its greater

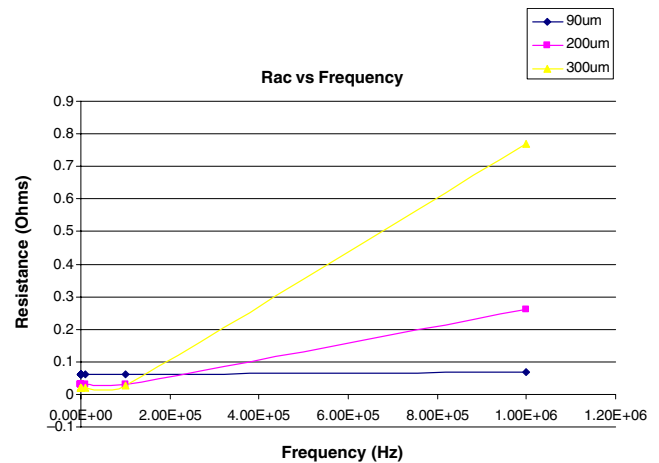


**Fig. 21** Winding resistance versus frequency for three cross-sections of windings



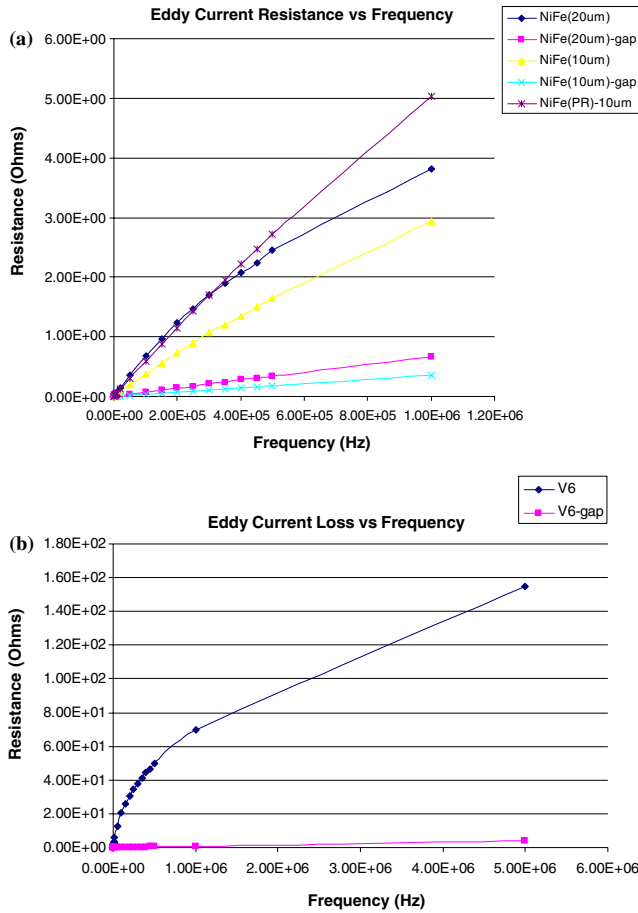


**Fig. 22** **a** Eddy current resistances versus frequency. **b** Eddy current losses versus frequency

resistivity but increased permeability makes it more susceptible to skin effects.

The impedance values of the various samples over the frequency range of interest increases linearly with frequency as shown in Fig. 23a and b. This indicates that parasitic capacitance effects are negligible and that the self resonant frequency has not yet been reached.

The  $Q$ -factor and inductance results are displayed in Fig. 24.

The  $Q$ -factor has a maximum value of 2 in the 500 kHz–1 MHz range. This is an indication that the core dimensions are acceptable for operation within this range. The  $Q$  factor changes as a function of frequency. At lower frequencies,  $Q$  is greater because only the DC resistance of the windings (which is very low) has an effect. As frequency goes up,  $Q$  will increase up to about the point where the skin effect and the combined distributed capacitances begin to dominate. Beyond this point,  $Q$  falls and will become zero at the self-resonant frequency.

The inductance of the devices is displayed in Fig. 25a and b. Variation of the inductance as a function of frequency occurs as the thickness of the respective cores approaches one skin depth. Without the inclusion of an

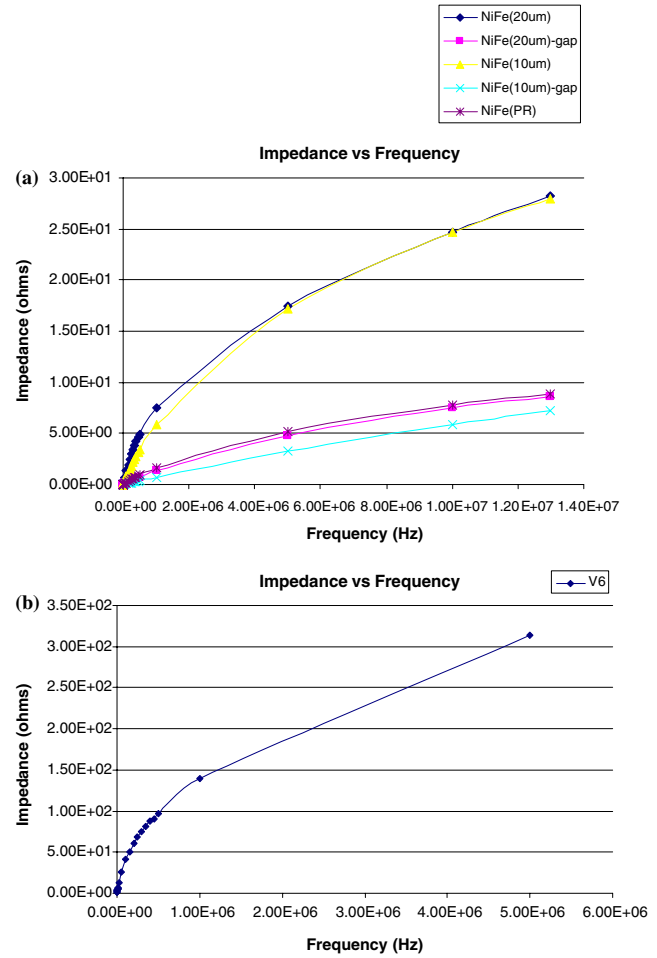


**Fig. 23** **a** Microinductor impedance versus frequency. **b** Microinductor impedance loss versus frequency

air gap the skin depth of the Vitrovac sample equals the core thickness at 6 kHz in comparison to 1 MHz with an air-gap. Therefore to operate with a constant inductance over a range of high frequencies, an air gap is mandatory for this material as shown by the graph (Fig. 25b).

Using Eq. 3 the theoretical DC saturation current of the NiFe is higher than the Vitrovac 6025 with and without an air-gap. It can therefore be concluded that NiFe cores perform notably better in applications requiring magnetic energy storage, such as in DC/DC converters. Applying Eq. 3 again the theoretical DC saturation current of the DC NiFe (10  $\mu$ m) sample is greater than its PR counterpart. Therefore it can be concluded that DC deposition within the chosen electrolyte composition produces a more favorable permalloy core than PR.

As an example to assess the performance of the device, the inductance of the 10  $\mu$ m thick NiFe (DC) core at 1 MHz is 0.9  $\mu$ H with an  $I_{\text{sat}}$  of 112 mA. The maximum voltage across the device is therefore

$$V = \frac{LI}{\lambda} = 100 \text{ mV} \quad (15)$$

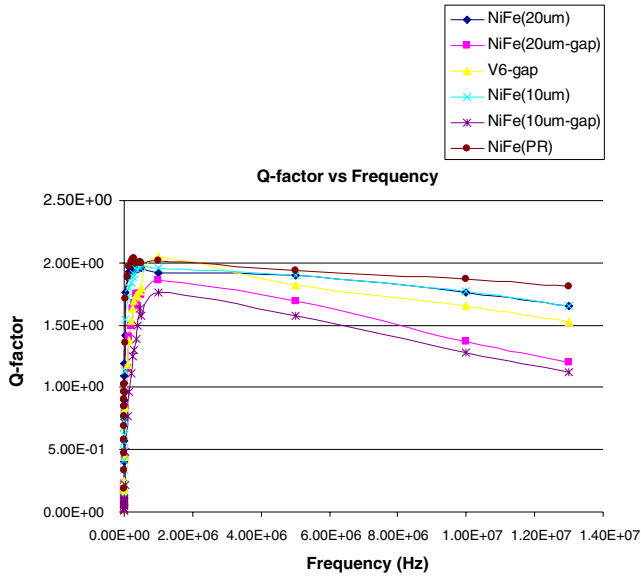


Fig. 24 Q-factor versus frequency

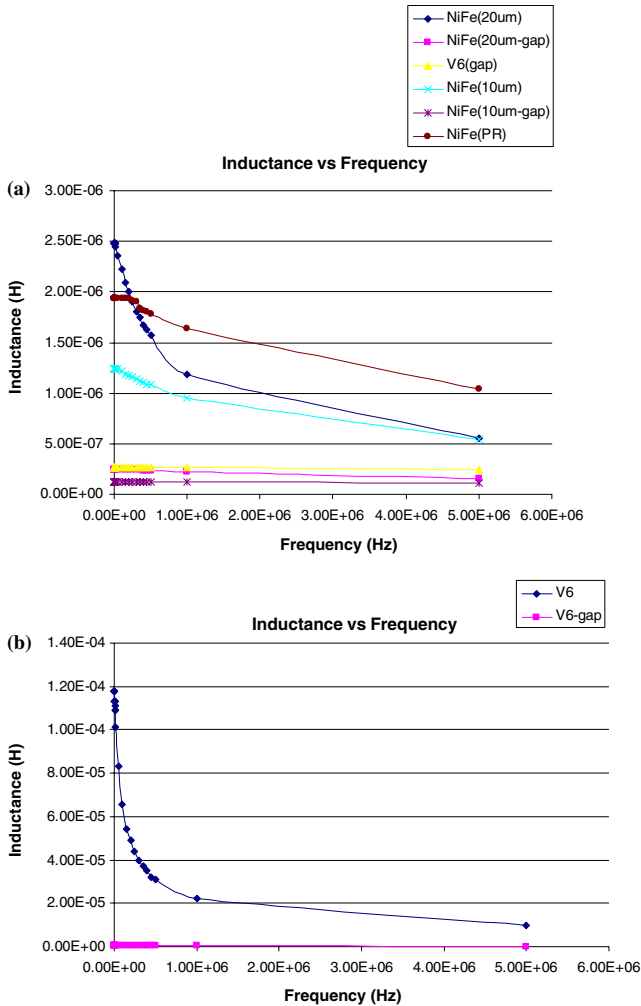


Fig. 25 a Inductance versus skin depth. b Inductance loss versus skin depth

and the output power is

$$P_{\text{out}} = V_{\text{out}} \times I_{\text{out}} = 11.3 \text{ mW} \quad (16)$$

To calculate the core loss the peak flux density within the core is calculated (Ludwig et al. 2003):

$$B_{pk} = \frac{V}{KNA_c f} = 0.15 \text{ T} \quad (17)$$

$K$  is a constant dependent on the waveform applied and in this instance a square wave is considered hence taking the value 4.

The core eddy current loss is added to the power dissipated by the windings according to the formula (Ludwig et al. 2003):

$$P_{\text{eddy}} = n \frac{(2\pi f B_{pk})^2 2XYh^3}{24\rho_s} = 2.03 \text{ } \mu\text{W} \quad (18)$$

where  $n$  is the number of laminate, in this case  $n = 1$ .  $X, Y$  and  $h$  are the dimensions of the core, and  $\rho_s$  is the core resistivity. In the same way the hysteresis losses can be calculated according to the formula (Ludwig et al. 2003):

$$P_{\text{hys}} = \frac{3}{2} XYh(4B_{pk}H_c) = 4.96 \times 10^{-16} \text{ W} \quad (19)$$

The Joule losses in the windings are:

$$P_{\text{Cu}} = I^2 R = 0.87 \text{ mW} \quad (20)$$

The overall efficiency,  $\eta$ , of the micro-inductor is therefore:

$$\eta = \frac{P_{\text{out}}}{(P_{\text{out}} + P_{\text{core}} + P_{\text{Cu}})} = 92.27\% \quad (21)$$

The power density is approximately  $4.12 \text{ W/cm}^3$ .

## 7 Conclusion

Micromachined inductors with different magnetic cores and geometries have been fabricated on glass using micromachined techniques borrowed from the LIGA process. By comparing microinductors with and without air-gaps in the core, it has been demonstrated that air-gap core devices exhibit improved characteristics.

From the results it can be concluded that parasitic capacitance between turns, turns to insulation layer, and turns to core do not appear to significantly affect inductor performance over the measured frequency range. It is evident that eddy currents and parasitic capacitance become significant at higher frequency. Eddy currents are the major core loss mechanism therefore the improvement in coercivity by PR which reduces hysteresis loss is negligible. The higher resistivity of the PR permalloy is attributed to the smaller grain which increases the grain boundary contribution, forming more tunneling barriers for carrier transport.

The results shown in the Figs. 21, 24a and 24b demonstrate that Eqs. 1 and 6 are only valid for uniform flux density and current flow, respectively. As a rule of thumb for laminated core, a laminate sheet should not have a thickness greater the skin depth for a given frequency.

The benefits of PR permalloy are reduced coercivity, increased resistivity, improved cross sectional area uniformity, and more variables are available to control the deposits characteristics. It was also noted that PR does not always improve current efficiency and increased overpotential does not always led to a reduction in grain size.

Observations of the effects on PR highlight that to avoid pitting a high cathodic to anodic current density ratio must be applied. Off-time is also an important parameter in attaining a pit free deposit since most of the samples with no off-time had the maximum amount of pits. The optimum waveform that produced nanocrystalline permalloy with good surface uniformity and no pitting was  $a=0.4$  mA,  $b=100$  ms,  $c=-0.6$  mA,  $d=10$  ms and  $e=10$  ms.

As a prototype the fabricated micro-inductor has proved that via an inexpensive UV LIGA and electroplating process, an efficient component can be fabricated. A novel UV-LIGA and flip chip fabrication process has been developed that permits the comparison of commercially available alloys and electroplated thin films. An optimal design process is to be developed and further work into core materials are to be performed.

**Acknowledgements** Thanks are extended to Prof. Cywinski for the VSM data performed at the University of Leeds, and to Raytheon Systems Limited for performing the resistivity measurements. This work was made possible through the financial support of EPSRC

through a CASE Industrial studentship and through the Scottish Manufacturing, the only Innovative Manufacturing Research Centre (IMRC) in Scotland.

## References

- Activities of the PFM on permalloy thin films deposition and magnetic devices (2000)
- Brunet M, O'Donnell T, O'Brien J, McCloskey P, O'Mathuna C (2001) Design study and fabrication techniques for high power density micro-transformers. In: Proceedings of 16th annual IEEE applied power electronics special conference
- Grandi G, Kazimierczuk MK, Massarini A, Reggiani U, Sancineto G (2004) Model of laminated iron-core inductors for high frequencies. *IEEE Trans Magnetics* 40(42):1839–1845
- Herzer G (1990) Grain size dependence of coercivity and permeability in nanocrystalline ferromagnets. *IEEE Trans Magn* 26:1397–1402
- Huljak RJ, Thottuvelil VJ, Marsh AJ, Miller BA (2000) Where are power supplies headed? In: Proceedings of Apec, pp 10–17
- Hurley WG, Gath E, Breslin JG (2000) Optimizing the AC resistance of multilayer transformer windings with arbitrary current waveforms. *IEEE Trans Power Electron* 15(2):369–376
- International technology roadmap for semiconductors (2001)
- Kazimierczuk MK, Sancineto G, Grandi G, Reggiani U, Massarini A (1999) High frequency small-signal model of ferrite core inductors. *IEEE Trans Magnetics* 35(5):4185–4189
- Lotfi AW, Wilkowski MA (2001) Issues and advances in high frequency magnetics for switching power supplies. *Proc IEEE* 89(6):833–845
- Ludwig M, Duffy M, O'Donnell T, McCloskey P, O'Mathuna SC (2003) Design study for ultra flat for PCB integrated inductors for low power conversion applications. *Trans Magn* 39(5): 3193–3195
- Matlosz M (1993) Competitive absorption effects in the electro-deposition of iron-nickel alloys. *J Electrochem Soc* 140:2272–2279
- Sasaki KY, Talbot JB (1995) Electrodeposition of binary iron-group alloys. *J Electrochem Soc* 143:3343–3348
- van Wyk JD, Lee FC (1999) Power electronics technology at the dawn of the New Millennium-Status and Future